Title	The Effect of crystal textures on the anodic oxidization of zirconium in a boiling nitric acid solution
Author(s)	Kato Chiaki, Ishijima Yasuhiro, Ueno Fumiyoshi, Yamamoto Masahiro
Citation	Journal of Nuclear Science and Technology, 53(9), p.1371-1379
Text Version	Author's Post-print
URL	https://jopss.jaea.go.jp/search/servlet/search?5054077
DOI	https://doi.org/10.1080/00223131.2015.1110506
Right	This is an Accepted Manuscript of an article published by Taylor & Francis in Journal of Nuclear Science and Technology on [date of publication], available online: http://www.tandfonline.com/10.1080/00223131.2015.1110506.

ARTICLE

The effect of crystal textures on the anodic oxidization of zirconium in a boiling nitric acid solution

Chiaki KATO[a*], Yasuhiro ISHIJIMA[a], Fumiyoshi UENO[a],

Masahiro YAMAMOTO[a]

[a] *Tokai Research and Development Center, Japan Atomic Energy Agency,*

2-4 Shirakata, Tokai-mura, Naka-gun, Ibaraki 319-1195, Japan

Abstract

The effects of crystal textures and the potentials in the anodic oxidation of zirconium in a boiling nitric acid solution were investigated to study the stress corrosion cracking of zirconium in nitric acid solutions. The test specimen was machined such that the specimen surface was parallel to the rolling surface, arranged with a (0002) crystal texture. The potentials applied for the anodic oxidation of zirconium were set at 1.2, 1.4, and 1.5 V against a saturated KCl–Ag/AgCl electrode (SSE) in boiling 6 M HNO_3. The growth of the zirconium oxide film dramatically changed depending on the applied potential at a closed depassivation potential (1.47 V vs. SSE in this study). At 1.5 V, the zirconium oxide film rapidly grows, and its growth exhibits cyclic oxidation kinetics in accordance with a nearly cubic rate law. The zirconium oxide film grows according to the quantity of electric charge, and the growth rate does not depend on the crystal texture in the pretransition region before the cyclic oxidation kinetics. However, the growth and cracking under the thick oxide film depend on the crystal texture in the transition region. On the normal direction (ND) side, the oxide film thickness decreases on average since some areas of the thick oxide

film are separated from the specimen surface owing to the cracks in the thick oxide. On the rolling direction (RD) side, no cracks in the thick oxide film are observed, but cracks are found under the thick oxide film, which deeply propagate in the metal matrix along the RD without an external stress. The cracks under the thick oxide film propagate to the center of the oxide layer. The crystal orientation relationship between the oxide layer and the zirconium matrix is $(0002)_{Zr}//(111)_{ZrO2}$, and the cracks in the oxide layer propagate in the $(0002)_{Zr}$ plane in the zirconium matrix. The oxide layer consists of string-like zirconium oxide and zirconium hydride. The string-like zirconium oxide contains orthorhombic ZrO_2 in addition to monoclinic ZrO_2. It is not well known why the cracks propagate along the $(0002)_{Zr}$ plane under the thick oxide film. As one assumption for the mechanism of crack initiation and propagation without an external stress, it is considered that the oxidizing zirconium hydrides precipitate in the $(0002)_{Zr}$ plane near the interface of the thick oxide film and the matrix. Then, the phase transformation from orthorhombic ZrO_2 to monoclinic ZrO_2 in the oxide layer causes the crack propagation in the (0002) plane.

Keywords; zirconium, nitric acid, cracking, corrosion, anodic oxidization, (0002) plane

---

* Corresponding author, E-mail: kato.chiaki16@jaea.go.jp

1. Introduction

Because zirconium has good corrosion resistance in severe corrosive environments, it has been used in chemical processing equipment requiring durability for corrosion.[1, 2] For corrosion resistance to a nitric acid solution, zirconium has been used in the major processing equipment of nuclear fuel-reprocessing plants adopting the PUREX process that contains a nitric acid solution to dissolve spent fuel and separate uranium and plutonium from the fuel.[3, 4] However, the susceptibility of stress corrosion cracking (SCC) has been reported for zirconium in a concentrated nitric acid solution.[5]

Kajimura *et al.* reported that the SCC susceptibility of zirconium in nitric acid solutions strongly depends on the potential and the orientation of the zirconium plate.[6] A nobler corrosion potential causes a breakdown in the passivated film and increases the SCC susceptibility in nitric acid solutions.[7] Recently, an investigation of the SCC of zirconium in nitric acid solutions concluded that the tarnish rupture of a grown thick zirconium oxide film during anodic oxidization is a convincing SCC mechanism.[8] However, the relationship between the orientation of the zirconium plate and the growth properties of the zirconium oxide film related to SCC was not fully studied.

The hexagonal close-packed (hcp) crystal structure is the stable structure of zirconium at standard temperature and pressure conditions, which develops preferred crystal orientations during fabrication processes, because the number of slip systems in the hcp crystal structure is limited.[9] Hence, the crystal textures of the zirconium plate strongly depend on the deformation direction such as the rolling direction (RD). This crystallographic anisotropy would cause changes in the SCC susceptibility during the oxidization of zirconium, depending on the orientation of the zirconium plate. In this study, the effect of the crystal

textures on the anodic oxidation of zirconium in boiling 6 M HNO_3 was investigated.

2. Experimental procedures

2.1. Preparation of the specimen

Pure zirconium (ASTM R 80702) was used as the test material in this study. ASTM R 80702 is used as equipment material for reprocessing plants in severely corrosive conditions. The zirconium plate used had a thickness of 8 mm by cold rolling and then annealing. The chemical compositions of the zirconium plate are listed with the typical compositions of the ASTM standard in **Table 1**.

<Table 1>

It was expected that the zirconium plate would have a crystalline anisotropy due to the crystal textures depending on the RD; thus, the crystal textures of the zirconium plate were preliminarily measured by X-ray diffraction. **Figure 1** shows the pole figures of the (0002) and $(10\bar{1}0)$ planes for the direction normal to the rolling surface of the zirconium plate.

<Figure 1>

The X-ray diffraction intensity of the (0002) plane was the strongest at the center of the pole figure. This diffraction pattern broadened to the transverse direction (TD). These results indicate that the (0002) plane is oriented to the normal direction (ND) side and slightly fluctuates to the TD. The X-ray diffraction intensity of the $(10\bar{1}0)$ plane was the strongest on the rolling direction (RD) sides of the pole figure. This indicates that the $(10\bar{1}0)$ plane is oriented to the ND side.

Figure 2 (a) and (b) show schematics of the electrode for the electrochemical tests and the machining orientation of the test specimen.

<Figure 2>

A disk-type specimen was used. The specimen has a diameter of 15 mm and a thickness of 3 mm. The specimens were polished using 600-grit emery paper. The specimen was fixed with a screw in a titanium rod and electrically connected to a potentiostat through the titanium rod. Polytetrafluoroethylene (PTFE) was used for electrical insulation and to seal the material in the specimen and in a glass tube. The disk surface was machined to be parallel to the rolling surface; therefore, the disk surface is the ND side having a (0002) orientation, which is the cleavage plane of zirconium. The specimens were cut in the middle to the RD after the corrosion tests in order to observe cross-sectional views of the oxide film on the RD side and ND side.

2.2. Electrochemical tests

2.2.1. Electrochemical measurement system

An integrated potentiostat equipped with a saturated KCl–Ag/AgCl (SSE) reference electrode was used for the electrochemical and anodic oxidation tests. **Figure 3** shows a schematic of the electrochemical measurement system in boiling nitric acid solutions.

<Figure 3>

To maintain electrical contact with the reference electrode in the boiling solution, a special junction was used. The junction had porous glass filters on both sides and contains a concentrated nitric acid solution (14 M HNO_3) as the junction electrolyte. The concentrated nitric acid solution was required to avoid electrical interruption due to bubble formation inside the junction at the boiling point of the test solutions. An intermediate vessel comprised the same test solution at room temperature. The potential shift in the junction at different temperatures was approximately less than 10 mV during the measurements.

2.2.2. Polarization curve measurements

The polarization curves of zirconium were measured in boiling 6 M HNO_3. The potential sweep rate for dynamic polarization was 20 mV/min. The depassivation potential was defined as the potential where the anodic current density rapidly increased.

2.2.3. Anodic oxidization

Anodic oxidization was performed in boiling 6 M HNO_3. The applied potentials were 1.2, 1.4, and 1.5 V vs. SSE. These potentials represented the passivated state and the transitions from the passivated state to the depassivated state observed by the polarization curve of zirconium. Anodic oxidization was performed for up to 500 h at 1.2 and 1.4 V. At 1.5 V, anodic oxidization was performed for up to 100 h because of the severe corrosion on zirconium in the depassivated state. The duration of anodic oxidization was changed to evaluate the growth of the oxide film for an increase in the total amount of electric charge.

2.3. Microscopic analysis of the oxide film

Macroscopic cross-sectional views of zirconium oxide on the RD and ND sides were observed using scanning electron microscopy (SEM). The average thickness of the oxide film was calculated as the area of the oxide layer in an SEM cross-sectional image unit (180 μm × 180 μm) divided by the width. The zirconium oxide film was analyzed using transmission electron microscopy (TEM) with selected area electron diffraction (SAD) patterns to understand the crystal structure of the film, which was microscopically ablated using a focused ion beam (FIB).

3. Results and discussion

3.1. Polarization curves

Figure 4 shows the anodic polarization curve of zirconium in boiling 6 M HNO_3.

<Figure 4>

A rapid increase in the current density was observed at the potential attributed to the transition from the passivated state to the depassivated state. The depassivation potential of zirconium in boiling 6 M HNO_3 was 1.47 V vs. SSE. This potential was near the depassivation potential that P. Fauvet reported.[10] The potentials applied during anodic oxidization are indicated on the anodic polarization curve in Fig. 4.

3.2. Anodic oxidizations

Figure 5 (a) and (b) show the typical current density–time curves and the total electric charge–time curves for the anodic oxidation of zirconium for 100 h.

<Figure 5>

At 1.2 V, the total amount of electric charge hardly increased with the elapsed time, and the total electric charge density after 100 h was approximately 0.2 C/cm^2 because the current density was consistently less than 1×10^{-6} A/cm^2. Zirconium had perfect corrosion resistance under these conditions. At 1.4 V, the total electric charge density increased with the elapsed time at an early stage, but this increase gradually stagnated. The total electric charge density after 100 h was approximately 5 C/cm^2 because the current density increased just after oxidation began to a maximum of 5×10^{-4} A/cm^2 and then decreased within several hours to less than 1×10^{-6} A/cm^2. Zirconium was slightly corroded under these conditions, but the corrosion resistance was maintained by a protective oxide film. At 1.5 V, the total amount of electric charge rapidly increased with time at an early stage, and cyclic corrosion kinetics were observed with several steps related to multiple current peaks. The maximum peak current density was 1.8×10^{-2}

A/cm^2, which was much larger than that at 1.4 V.

3.3. The average thickness of the oxide film

Macroscopic cross-sectional views of the zirconium oxide film were obtained in order to understand the oxidation processes. **Figure 6** shows the cross-sectional back-scattered electron (BSE) images of the ND and RD sides after anodic oxidization at 1.4 V and 1.5 V.

<Figure 6>

In the BSE image, the dark contrast parts are identified as zirconium oxide, ZrO_2, by SEM–EDS (energy dispersive X-ray spectroscopy). **Figure 7** shows the relationship between the total amount of electric charge and the average thickness of the oxide film on the ND and RD sides measured from the cross-sectional images.

<Figure 7>

At 1.2 V, the thickness could not be measured because the oxide film was too thin. At 1.4 V, oxide parts with spots were observed on both sides, and no differences in their average thickness were observed. The average thickness was approximately 6 μm at 4.5 C/cm^2, where the oxidation time was 500 h. Cracks were slightly observed between the oxide film and the matrix, but no cracks were observed in the middle of the oxide film. At 1.5 V, the thickness increased as the total electric charge density increased up to 15 C/cm^2. This increase in the oxide film thickness is independent of the potentials, and there were no differences for both sides.

It is considered that the zirconium oxide film grew according to the amount of electric charge, and the growth did not depend on the crystal texture in the pretransition region before the cyclic oxidation kinetics. In contrast, an increase in the thickness was suppressed over 120 C/cm^2 at the end of the pretransition

region, where the oxidation time was 10 h, and differences in the oxide growth were observed on both sides. The thickness on average on the ND side decreased at 500 C/cm^2 in the transition region at 100 h. Many cracks were observed in the middle of the layer, and some areas of the thick oxide film separated from the specimen surface on the ND side. The cracks in the oxide film tended to layer along the RD, and the layered cracks along the RD bridged each other. In addition, an oxide layer along the RD in the matrix was observed under the thick oxide film.

On the RD side, the thickness of the oxide film hardly changed over 120 C/cm^2, and the thickness was approximately 120 μm, which is thicker than that on the ND side. Cracks in the oxide film and the separated oxide film, as on the ND side, were not observed. In addition, several cracks in the metal matrix were observed on the RD side under the thick oxide film, which deeply propagated to the RD without an external stress. These results show that cracks easily occur along the RD; then, the crack propagation depending on the crystal texture in the zirconium plate causes a difference in the crack formation in the thick oxide film on the RD and ND sides.

3.5. The cracks under the thick oxide film on the RD side

At 1.5 V, several cracks were observed in the metal matrix on the RD side under the thick oxide film, which deeply propagated to the RD without an external stress. These cracks clearly depended on the crystal texture because the (0002) plane is located with the RD in the crystal texture (see Fig. 2).

In order to understand the crack propagation process, the time at which the deeply propagated crack occurs under the thick oxide film was investigated. **Figure 8** (a), (b), and (c) show cross-sectional SEM–BSE images of the specimens on the RD side for total amounts of electric charge of 15, 120, and 250 C/cm^2 at 1.5

V, which are at anodic oxidation times of 1, 10, and 24 h.

<Figure 8>

At 15 C/cm^2 in the pretransition region, zirconium was partially oxidized. At 120 C/cm^2 at the end of the pretransition region, the oxide film thickened, and a portion of the oxide penetrated with a crack was observed under the thick oxide film. At 250 C/cm^2 in the transition region, the cracks propagated to the RD from the penetrated oxide portion. The crack tip was surrounded with a thin oxide layer (i.e., the oxide crack), and the oxide crack consisted of many string-like oxides along the direction of crack propagation. These string-like oxides were only observed at the interface of the thick oxide film and the matrix. It is assumed that the string-like oxide initiates the oxide crack.

3.4. TEM analysis of the oxide crack tip

To understand the morphology and crystallographic orientation of the oxide crack initiation, the oxide crack tip was analyzed using TEM. **Figure 9** (a) and (b) show an SEM image of the FIB-sampled area in the oxide crack tip and a TEM image of the oxide crack tip, where the broken-line box in Fig. 9(a) denotes the TEM observation area.

<Figure 9>

A crack propagating to the RD was observed at the center of the oxide layer containing the string-like zirconium oxides. The oxide layer consisted of many string-like oxides including microcracks, as shown in Fig. 9(b). The texture of the string-like oxides was along the RD.

The broken circles in Fig. 9(b) indicate the areas analyzed for the SAD patterns of the matrix (SAD1) and the oxide layer involved with the matrix (SAD2). **Figure 10** shows the diffraction patterns of SAD1 and SAD2.

<Figure 10>

The direction of incidence of the electron beam was $[\bar{1}100]$. The diffraction patterns of the (0002) plane of the matrix, SAD1, were completely arranged along the dash–dot line indicating the ND. This result shows that the (0002) plane of zirconium is assigned to the RD and supports the crystal structure of the zirconium plate in the pole figure. The diffraction patterns in the oxide layer, SAD2, imply a few crystal structures. At least three crystal structures were confirmed in the oxide layer, which were hexagonal Zr, monoclinic ZrO_2, and tetragonal ZrH_2. The spots of $(111)_{ZrO2}$ were arranged on the ND, indicating a $(0002)_{Zr}//(111)_{ZrO2}$ crystal orientation. These results indicate that there is crystallographic relationship between zirconium oxide and the zirconium matrix, and cracks easily propagate along the (0002) plane in the zirconium matrix. It is unclear why zirconium hydride coexists in the oxide layer formed during anodic oxidization in the nitric acid solution. The calculated equilibrium potential of zirconium hydride of –0.8 V (vs. NHE) at pH = 0 is much less noble than the applied potential.[11] It is assumed that zirconium hydride is unstable and easily oxidized under these conditions.

Other crystal structures in addition to hexagonal Zr, monoclinic ZrO_2, and tetragonal ZrH_2 were observed in the oxide layer. Therefore, the oxide layer containing the string-like oxide was analyzed in detail by using narrow-area electron diffraction (NAD). **Figure 11** shows a TEM dark-field image of the oxide layer and the diffraction patterns of the analyzed positions (NAD1, NAD2, and NAD3).

<Figure 11>

The dark-field image is useful for observing the differences in the crystal structure. NAD1 is the point corresponding to the string-like oxide near the boundary between the oxide layer and the matrix. Further, NAD2 is the point

corresponding to the nonoxidized layer between the string-like oxides. Finally, NAD3 is the point corresponding to the string-like oxide near a microcrack.

The diffraction pattern of orthorhombic ZrO_2, which is indicated by the weak spots in Fig. 11, was confirmed in addition to monoclinic ZrO_2 for NAD1. It has been reported that orthorhombic ZrO_2 is the stable phase for zirconium oxide under a high compressive stress, and the compressive stress in the oxide film causes a phase change from monoclinic ZrO_2 to orthorhombic ZrO_2.[12] It is well known that the extreme compressive stress in the oxide film is caused by the growth of the zirconium oxide film because of the high volume dilation ratio in the ZrO_2/Zr system.[13] The accumulated compressive stress in the oxide film depends on the thickness of the oxide film, thereby causing a change in the volume dilation upon oxide formation.[14, 15, 16] Therefore, it is reasonable that a phase transition in the zirconium oxide layer can occur under the thick oxide film.

The diffraction pattern of tetragonal ZrH_2 was confirmed in NAD2, i.e., the nonoxidized layer between the string-like oxides. The spots of $(001)_{ZrH2}$ were arranged on the ND, indicating a $(0002)_{Zr}//(001)_{ZrH2}$ crystal orientation and that zirconium hydride precipitates in the $(0002)_{Zr}$ plane. This reason why zirconium hydride coexists in the string-like oxide layer remains an issue for further study. However, it might be possible to form zirconium hydride in zirconium oxide because it is well known that zirconium hydride is formed by oxidizing Zircaloy (a zirconium alloy containing 98 wt% zirconium) in high-temperature water and the zirconium hydride precipitates on the $(0002)_{Zr}$ plane.[17]

The diffraction pattern of monoclinic ZrO_2 was confirmed in NAD3, i.e., the string-like oxide near the microcrack. The spots of $(110)_{ZrO2}$ did not match the ND, and orthorhombic ZrO_2 was not observed. It is assumed that these results

show the transformation of initially orthorhombic ZrO_2 to monoclinic ZrO_2 and the crystal rotation caused by the microcrack.

It is well known that the transformation from the tetragonal phase to the monoclinic phase causes cracking in the zirconium oxide film in high-temperature water, as found in reactor conditions.[18, 19] Tetragonal ZrO_2 is the stabile phase at high temperatures instead of orthorhombic ZrO_2, and the molar volume of monoclinic ZrO_2 is greater than that of orthorhombic ZrO_2.[12] It has been reported that tetragonal ZrO_2 can be the dominant phase close to the metal/oxide interface in the scales formed on zirconium alloys, and the tetragonal phase transforms to the monoclinic phase after fracture with cracking in the oxide film.[18]

These reports support the fact that that the volume expansion due to the phase transformation from orthorhombic ZrO_2 to monoclinic ZrO_2 causes crack initiation in the oxide layer in this study.

3.5. The anodic oxidation process of zirconium

The zirconium oxidation process strongly depended on the potential during anodic oxidization, as the zirconium oxide film grows according to the amount of electric charge. At 1.2 V, which is less than the depassivation potential (1.47 V in this study), the oxide film hardly grows. Moreover, the growth rate of the oxide film dramatically changed at the closed depassivation potential and depended on the applied potential. At 1.4 V, which is slightly less than the depassivation potential, the oxide film grew, but the growth stops at an early stage. In contrast, the oxide film rapidly grows at 1.5 V, which is slightly greater than the depassivation potential, and the growth clearly reveals the cyclic oxidation kinetics in accordance with a nearly cubic rate law.

In corrosion studies of Zircaloy, cyclic corrosion kinetics with a nearly cubic

rate law have been revealed.[19] These cyclic kinetics are caused by destabilization of the oxide film; as a result, the oxide film grows, accumulates compressive stress as the oxide thickness increases, and fractures with cracking at the end of the cycle.

Figure 12 shows schematics of the oxidation process of zirconium at 1.5 V.

<Figure 12>

The zirconium oxide film is partially oxidized at an early stage of the pretransition region, and the oxide film then grows and does not depend on the crystal texture according to the amount of electric charge. At the end of the pretransition region, cracking in the oxide film occurs as a result of destabilization in zirconium oxide. On the ND side, cracks in the oxide film tended to layer along the RD, and the layered cracks along the RD bridged each other. On the RD side, the cracks along the RD penetrated the oxide portion under the thick oxide film. As a result of the SEM/TEM analysis of the oxide crack tip along the RD, cracking occurred at the center of the oxide layer, including many string-like zirconium oxides and hydrides. The string-like oxides and hydrides are arranged in the (0002) plane in the zirconium matrix, and the string-like oxides consist of monoclinic ZrO_2 and orthorhombic ZrO_2. The transformation from orthorhombic ZrO_2 to the monoclinic phase causes crack initiation in the zirconium oxide film.

For the transition revealing the cyclic oxidation kinetics, many cracks occurred at the boundary between the oxide film and the zirconium matrix. On the ND side, some areas of the thick oxide film separated from the specimen surface. This separation causes the cyclic oxidation kinetics, which are explained by the destabilization of the oxide film, similar to the corrosion studies of Zircaloy. On the RD side, cracks propagated in the metal matrix under the thick oxide film,

which deeply propagate along the RD without an external stress. It is not well known why cracks propagate along the (0002) plane in the zirconium matrix under the thick oxide film. As one assumption for the mechanism of crack initiation and propagation without an external stress, it is considered that oxidizing zirconium hydrides precipitated in the $(0002)_{Zr}$ plane near the interface of the thick oxide film and the matrix. Then, the phase transition from orthorhombic ZrO_2 to monoclinic ZrO_2 in the oxide layer caused crack propagation in the $(0002)_{Zr}$ plane without an external stress. As another possibility, the asymmetric stress state on the ND and RD sides might cause the crack propagation along the RD because of the stress relaxation in the oxide film on the ND side due to the separation of the oxide layer. It would be necessary to evaluate the stress state near the oxide crack by kernel averaged misorientation (KAM) using electron backscatter diffraction (EBSD) for the support of the another possibility. This is planned for future work.

5. Conclusions

The anodic oxidization of zirconium was performed in boiling 6 M HNO_3. The effect of the crystal texture and applied potential on the anodic oxidation of zirconium was investigated. The following results were obtained:

1. The growth of the zirconium oxide film dramatically changes depending on the applied potential at the closed depassivation potential (1.47 V vs. SSE in this study). At 1.2 V, zirconium has excellent corrosion resistance. At 1.4 V, zirconium slightly corrodes, but the corrosion resistance is maintained by the protective oxide film. At 1.5 V, the zirconium oxide film rapidly grows, and the growth reveals the cyclic oxidation kinetics in accordance with a nearly cubic rate law.

2. The zirconium oxide film grows according to the total amount of electric charge, and the growth does not depend on the crystal texture in the pretransition region before the cyclic oxidation kinetics; however, the growth depends on the crystal texture after the pretransition region. On the ND side, cracks occur in the middle of the oxide film, and some areas of the thick oxide film are separated from the specimen surface. On the RD side, separation of the oxide film does not occur, but several cracks are observed under the thick oxide film, which deeply propagate in the metal matrix along the RD without an external stress.
3. The cracks under the thick oxide film on the RD side propagate to the center of the oxide layer. The crystal orientation relationship between the oxide layer and the zirconium matrix is $(0002)_{Zr}//(111)_{ZrO2}$, and the cracks in the oxide layer propagate in the (0002) plane in zirconium matrix.
4. The oxide layer consists of string-like zirconium oxide and hydride. The string-like zirconium oxide contains orthorhombic ZrO_2 in addition to monoclinic ZrO_2. It is not well known why the cracks propagate along the (0002) plane in the zirconium matrix under the thick oxide film. As one assumption for the mechanism of crack initiation and propagation without an external stress, it is considered that the oxidizing zirconium hydrides precipitated in the $(0002)_{Zr}$ plane at the interface of the thick oxide film and the matrix, and then, the phase transition from orthorhombic ZrO_2 to monoclinic ZrO_2 in the oxide layer causes crack initiation and propagation in the (0002) plane without an external stress.

REFERENCES

1. Knittel D, Webster R. Corrosion Resistance of Zirconium and Zirconium Alloys in Inorganic Acids and Alkalies: ASTM; 1981.

2. Moniz BJ. Corrosion Resistance of Zirconium in Chemical Processing Equipment. Webster R, Young C, editors: ASTM; 1984.

3. Andreeva VV, Glukhova AI. Corrosion and Electrochemical Properties of Titanium, Zirconium and Titanium-Zirconium Alloys in Acid Solutions. II. Journal of Applied Chemistry. 1962;12:457-68.

4. Golden LB, Lane IR, Acherman WL. Corrosion Resistance of Titanium, Zirconium, and Stainless Steel. Industrial & Engineering Chemistry. 1952;44:1930-9.

5. Beavers JA, Griess JC, Boyd WK. Stress Corrosion Cracking of Zirconium in Nitric Acid. Corrosion. 1981;36:292-7.

6. Kajimura H, Nagano H. Stress Corrosion Cracking of Zirconium in Hot Nitric Acid. Corrosion. 1992;48:391-7.

7. Kajimura H, Nagano H. Passivity and its Breakdown on Zirconium in High Temperature Nitric Acid. Corrosion Science. 1990;31:261.

8. Ishijima Y, Kato C, Motooka T, Yamamoto M, Kano Y, Ebina T. Stress Corrosion Cracking Behavior of Zirconium in Boiling Nitric Acid Solutions at Oxide Formation Potentials. Materials Transactions. 2013;54:1001-5.

9. Tenckhoff E. Deformation Mechanisms, Texture, and Anisotropy in Zirconium and Zircaloy: ASTM; 1988.

10. Fuvet P. Corrosion Issues in Nuclear Fuel Reprocessing Plants. In: Feron D, editor. Nuclear Corrosion Science and Engineering: Woodhead Publishing; 2012. p. 679-728.

11. Chemical Reaction and Equilibrium Software HSC Chemistry 6. Eastern Finland: Outotec.

12. Ohtaka O, Yamanaka T, Kume S, Ito E, Navrotsky A. Stability of Monoclinic and Orthorhombic Zirconia: Studies by High-Pressure Phase Equilibria and Calorimetry. Journal of the

American Ceramics Society. 1991;74:505-9.

13. Parise M, Sicardy O, Cailletaud G. Modelling of the Mechanical Behavior of the Metal-Oxide System During Zr Alloy Oxidation. Journal of Nuclear Materials. 1998;256:35-46.

14. Overmeere QV, Proost J. Stress-Induced Breakdown During Galvanostatic Anodising of Zirconium. Electrochimica Acta. 2010;55:4653-60.

15. Archibald LC, Leach JSL. The Anodic Oxidation of Zirconium - I. Growth Stresses in Anodic ZrO_2 Films. Electrochimica Acta. 1977;22:15-20.

16. Overmeere QV, Proost J. Stress-Affected and Stress-Affecting Instabilities During the Growth of Anodic Oxide Films. Electrochimica Acta. 2011;56:10507-15.

17. Une K, Nogita K, Ishimoto S, Ogata K. Crystallography of Zirconium Hydrides in Recrystallized Zircaloy-2 Fuel Cladding by Electron Backscatter Diffraction. Journal of Nuclear Science and Technology. 2004;41:731-40.

18. Goldlewski J, Gros JP, Lambertin M, Wadier JF, Weidinger H. Raman Spectroscopy Study of the Tetragonal-to-Monoclinic Transition in Zirconium Oxide Scales and Determination of Overall Oxygen Diffusion by Nuclear Microanalysis of O18. In: Eucken CM, Garde AM editors. Philadelphia: Publisher; 1991.

19. Pilling NB, Bedworth RE. Journal of the Institute of Metals. 1923;29:529.

Figure and table

Table 1 Chemical composition of the zirconium plate (mass%)

Figure 1 (a) and (b) Pole figures of the (0002) and $(10\bar{1}0)$ planes for the direction normal to the rolling surface, as measured by X-ray diffraction.

Figure 2 Schematics of (a) the specimen during anodic oxidization and (b) the machining orientation of the specimen and crystal orientation of the Zr plate.

Figure 3 Schematic of the electrochemical cell system for the boiling nitric acid solution.

Figure 4 Anodic polarization curve of zirconium in a boiling nitric acid solution. I is the current density, and E is the potential.

Figure 5 (a) Typical current density–time curves and (b) the total electric charge–time curves during the anodic oxidation of zirconium in boiling 6 M HNO_3. I is the current density, Q is the total amount of electric charge, and t is the time.

Figure 6 Cross-sectional SEM–BSE images of the specimen after the anodic oxidation of zirconium at 1.4 V and 1.5 V.

Figure 7 Relationship between the average thickness of the oxide film and the total amount of electric charge during the anodic oxidation of zirconium in boiling 6 M HNO_3. Q is the electric charge, and d_{oxide} is the average thickness of the oxide film.

Figure 8 Cross-sectional SEM–BSE images on the RD side after the anodic oxidation of zirconium at (a)15 C/cm^2 [1 h], (b) 120 C/cm^2 [10 h], and (c) 250 C/cm^2 [25 h] at 1.5 V.

Figure 9 (a) SEM image of the FIB-sampled area in the oxide crack tip similar to Fig. 8(c) and (b) TEM image of the oxide crack tip.

Figure 10 (a) Selected-area electron diffraction patterns of the matrix (SAD1) and (b) selected-area electron diffraction patterns of the oxide in the oxide crack tip (SAD2). The open arrows, open circles, and open triangles correspond to Zr (hexagonal), ZrO_2 (monoclinic), and ZrH_2 (tetragonal).

Figure 11 (a) TEM dark-field image for the center of SAD2 in Fig. 9(b), (b) narrow-area electron diffraction patterns of NAD1 at the string-like oxide, (c) NAD2 at the nonoxidized layer between the string-like oxides, and (d) NAD3 at the string-like oxide beside a macrocrack. The open circles, open arrows, and open triangles correspond to ZrO_2 (monoclinic), ZrO_2 (orthorhombic), and ZrH_2 (monoclinic).

Figure 12 Schematic of the oxidation process of zirconium at 1.5 V and the mechanism of crack initiation and propagation in the (0002) plane in the zirconium matrix without an external stress.

Table 1 Chemical composition of the zirconium plate (mass%)

	H	C	N	O	Fe+Cr	Hf	Zr+Hf
Zr plate	<0.0004	0.02	0.005	0.14	0.08	0.8	Bal.
ASTM B551 R60702	<0.005	<0.05	<0.025	<0.16	<0.2	<4.5	>99.2

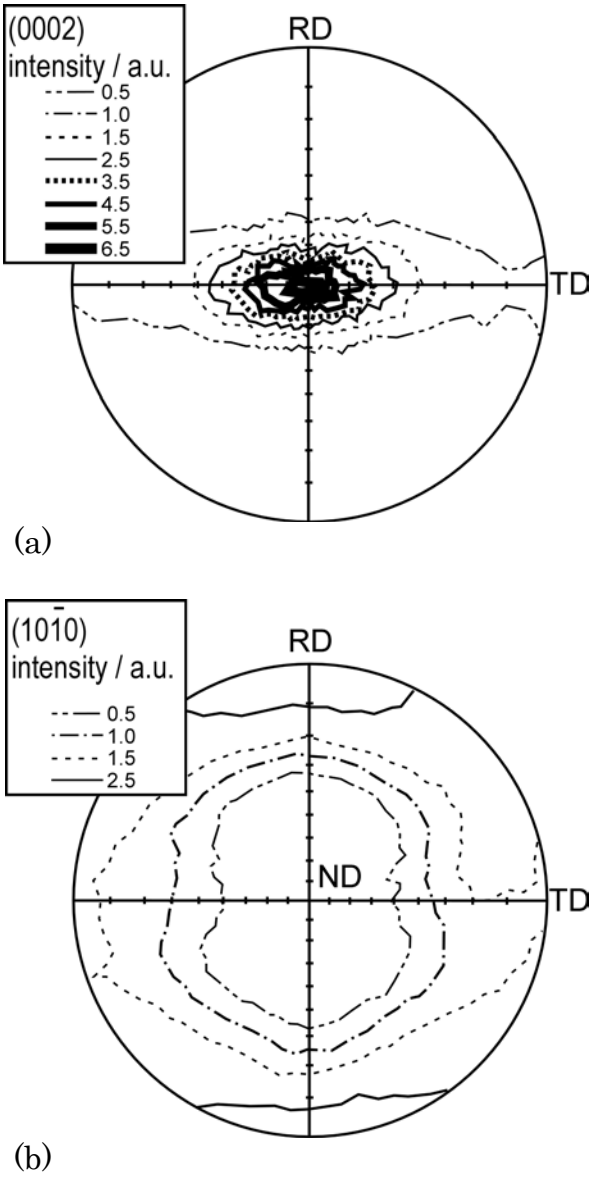

Figure 1 (a) and (b) Pole figures of the (0002) and (10$\bar{1}$0) planes for the direction normal to the rolling surface, as measured by X-ray diffraction.

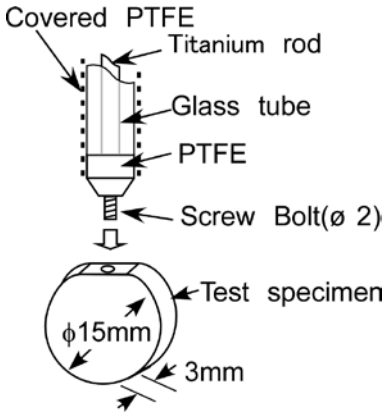

(a)

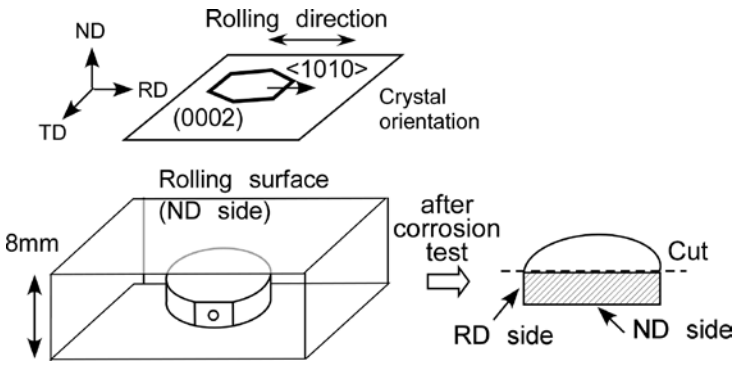

(b)

Figure 2 Schematics of (a) the specimen during anodic oxidization and (b) the machining orientation of the specimen and crystal orientation of the Zr plate.

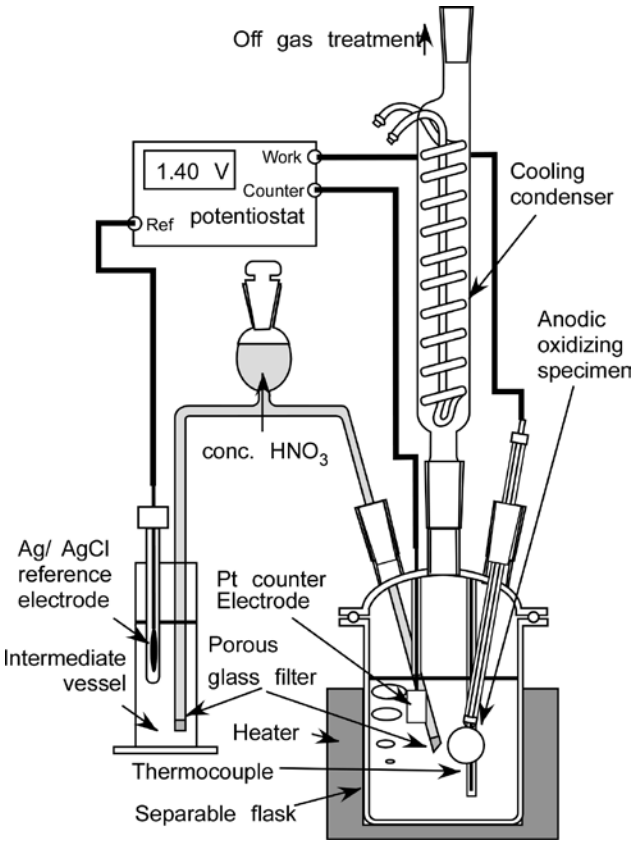

Figure 3 Schematic of the electrochemical cell system for the boiling nitric acid solution.

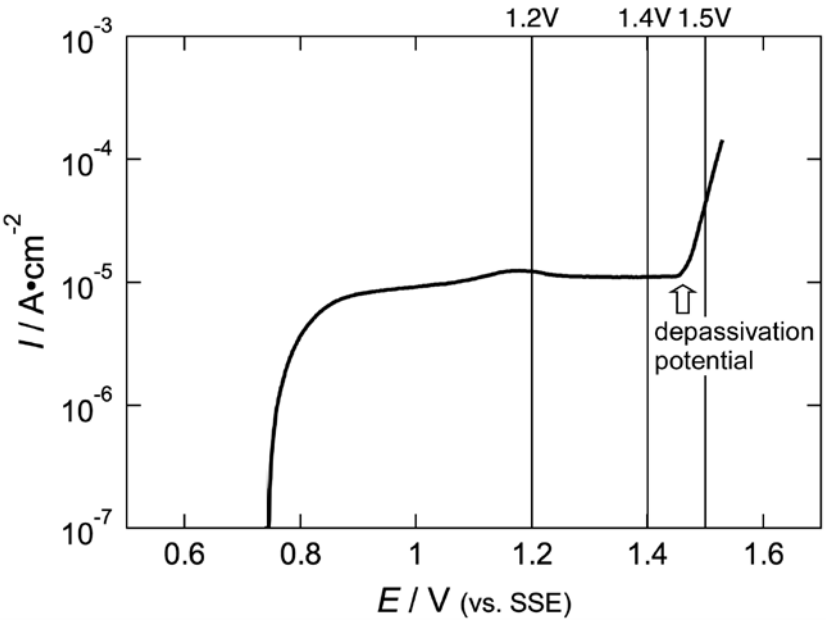

Figure 4 Anodic polarization curve of zirconium in a boiling nitric acid solution. I is the current density, and E is the potential.

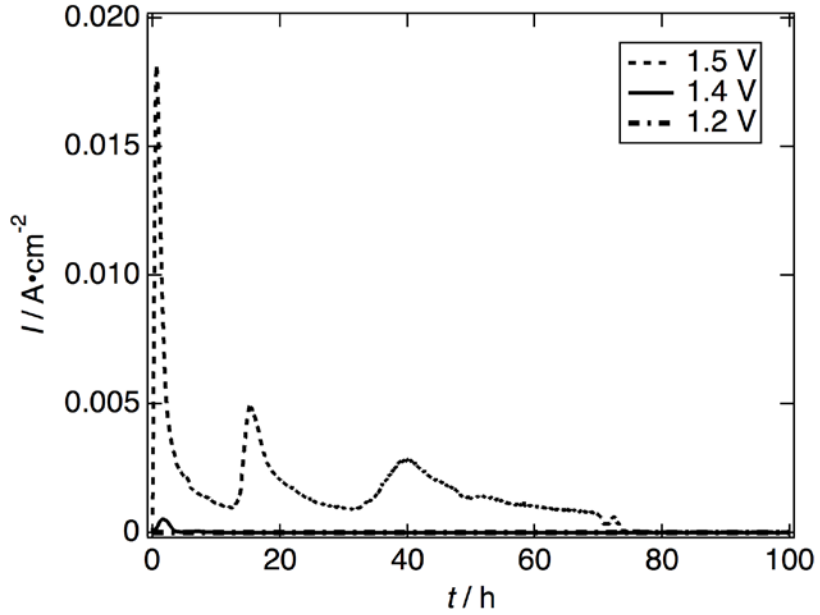

(a)

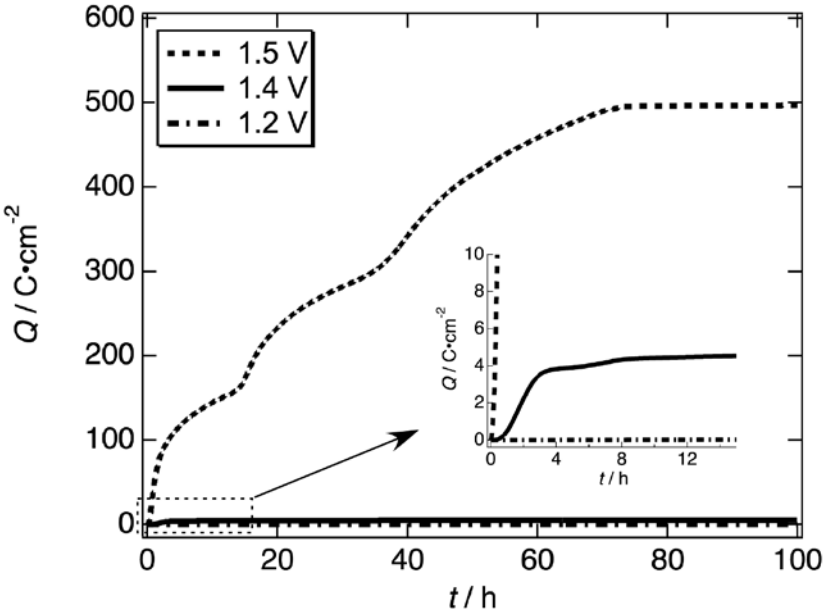

(b)

Figure 5 (a) Typical current density–time curves and (b) the total electric charge–time curves during the anodic oxidation of zirconium in boiling 6 M HNO_3. I is the current density, Q is the total amount of electric charge, and t is the time.

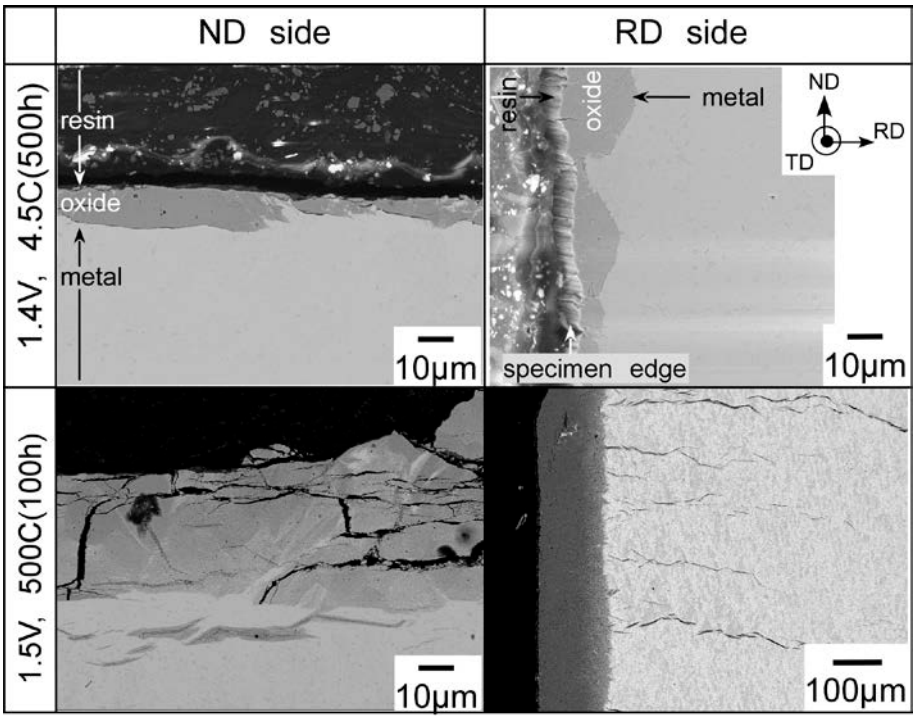

Figure 6 Cross-sectional SEM–BSE images of the specimen after the anodic oxidation of zirconium at 1.4 V and 1.5 V.

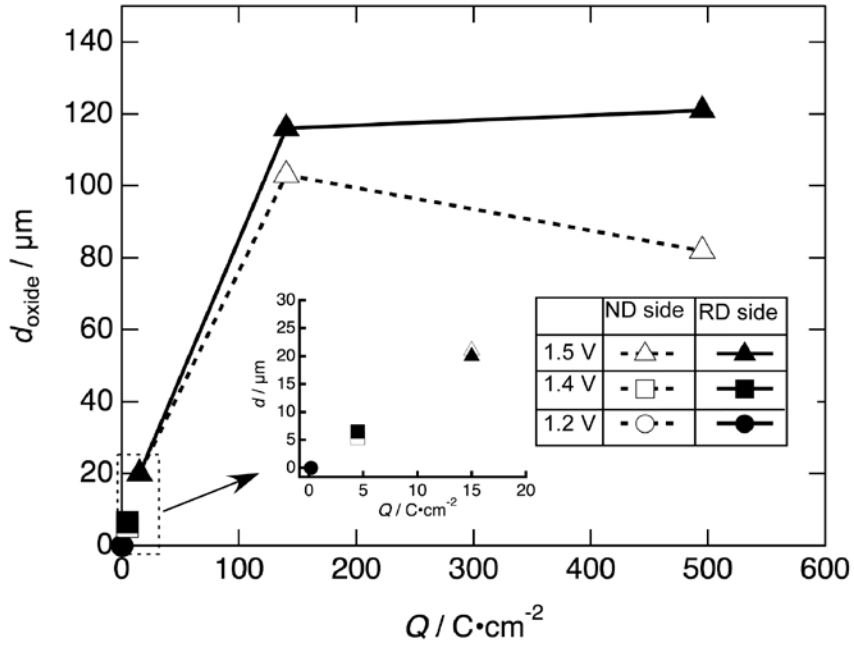

Figure 7 Relationship between the average thickness of the oxide film and the total amount of electric charge during the anodic oxidation of zirconium in boiling 6 M HNO_3. Q is the electric charge, and d_{oxide} is the average thickness of the oxide film.

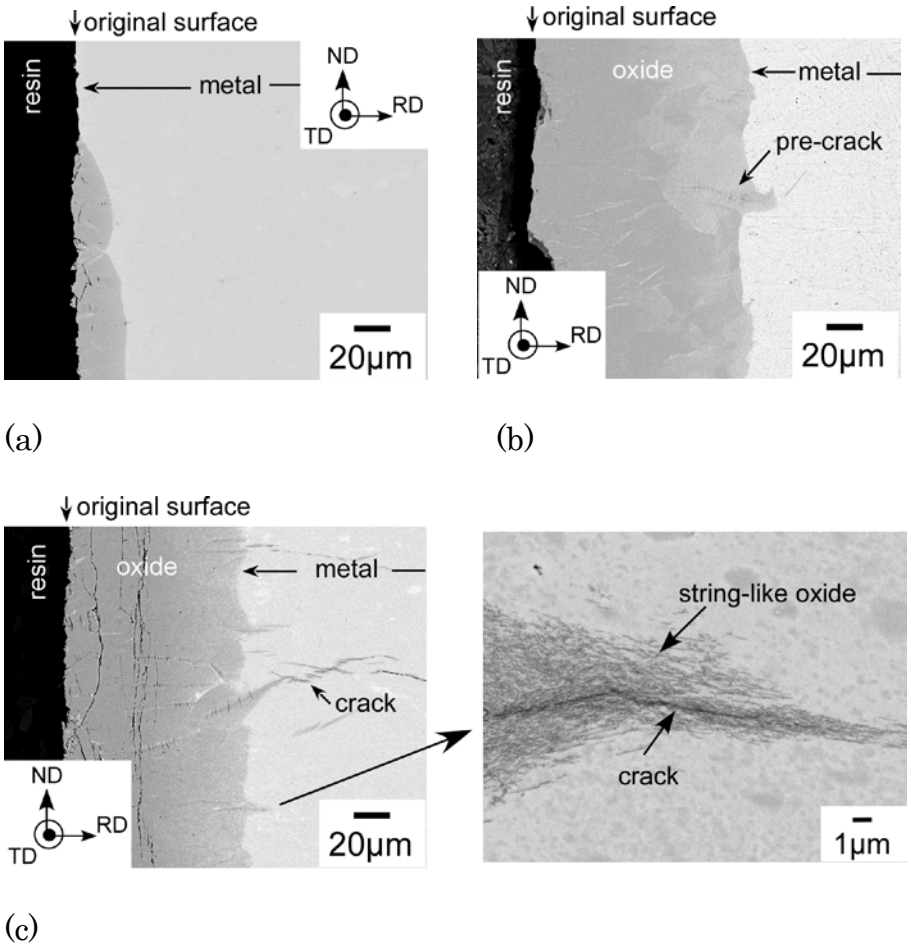

Figure 8 Cross-sectional SEM–BSE images on the RD side after the anodic oxidation of zirconium at (a)15 C/cm^2 [1 h], (b) 120 C/cm^2 [10 h], and (c) 250 C/cm^2 [25 h] at 1.5 V.

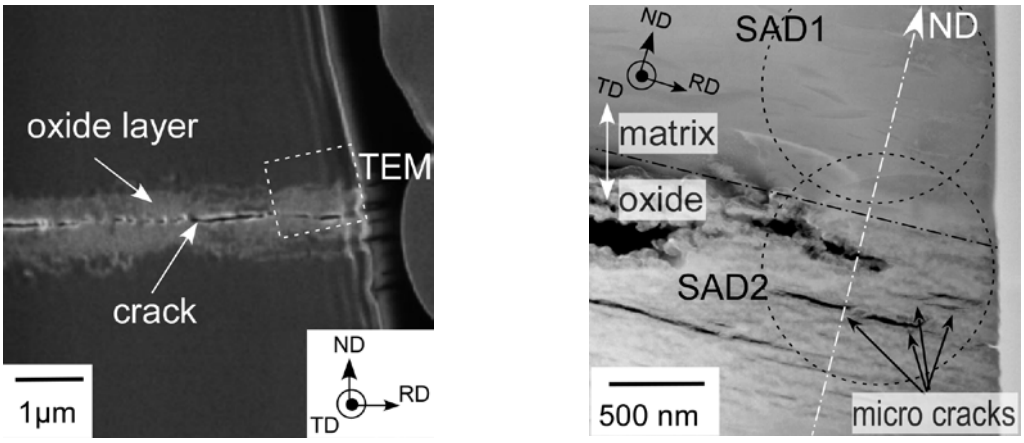

(a) (b)

Figure 9 (a) SEM image of the FIB-sampled area in the oxide crack tip similar to Fig. 8(c) and (b) TEM image of the oxide crack tip.

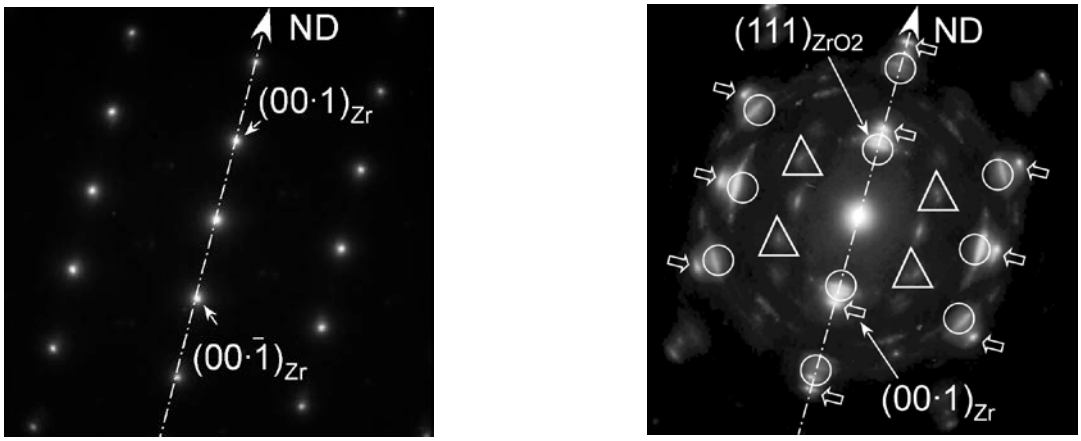

(a) (b)

Figure 10 (a) Selected-area electron diffraction patterns of the matrix (SAD1) and (b) selected-area electron diffraction patterns of oxide in the oxide crack tip (SAD2). The open arrows, open circles, and open triangles correspond to Zr (hexagonal), ZrO_2 (monoclinic), and ZrH_2 (tetragonal).

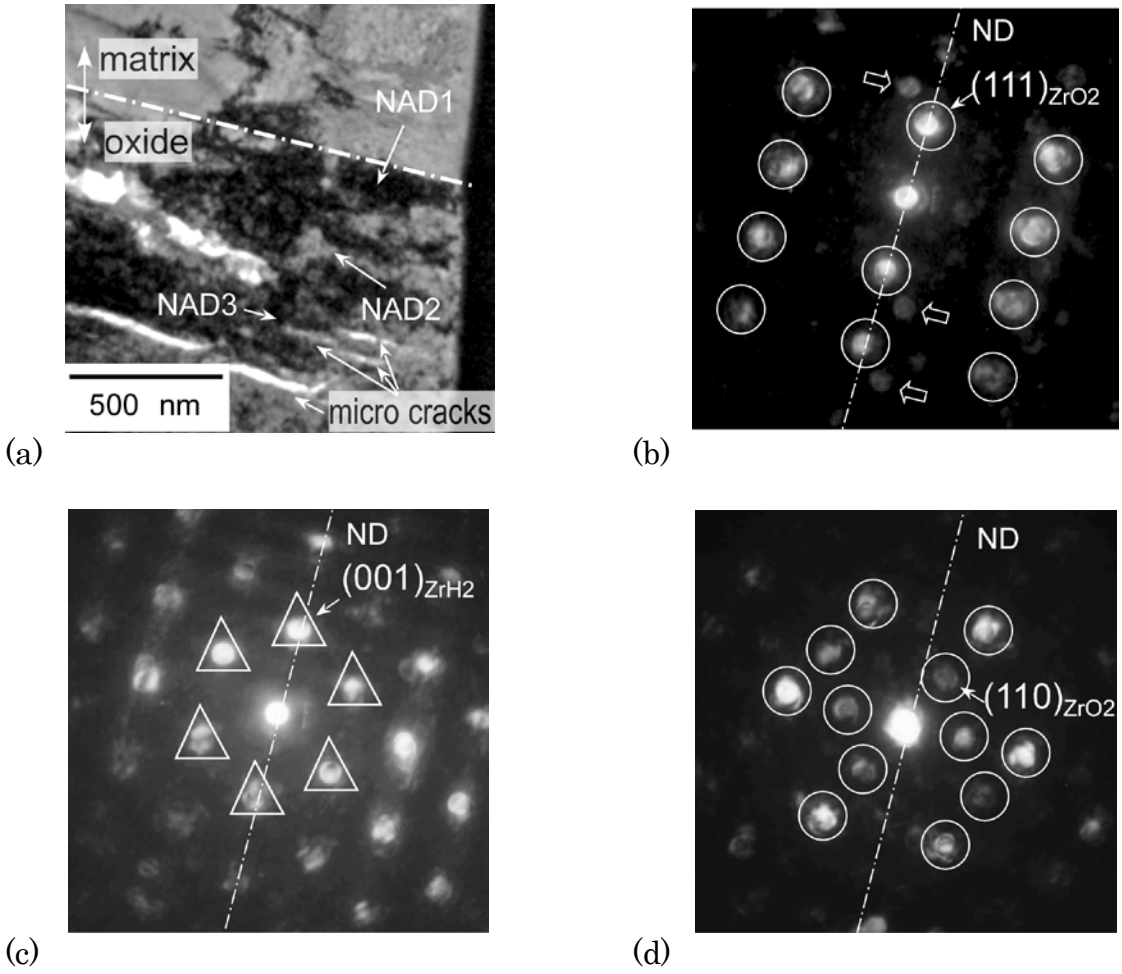

Figure 11 (a) TEM dark-field image for the center of SAD2 in Fig. 9(b), (b) narrow-area electron diffraction patterns of NAD1 at the string-like oxide, (c) NAD2 at the nonoxidized layer between the string-like oxides, and (d) NAD3 at the string-like oxide beside a macrocrack. The open circles, open arrows, and open triangles correspond to ZrO_2 (monoclinic), ZrO_2 (orthorhombic), and ZrH_2 (tetragonal).

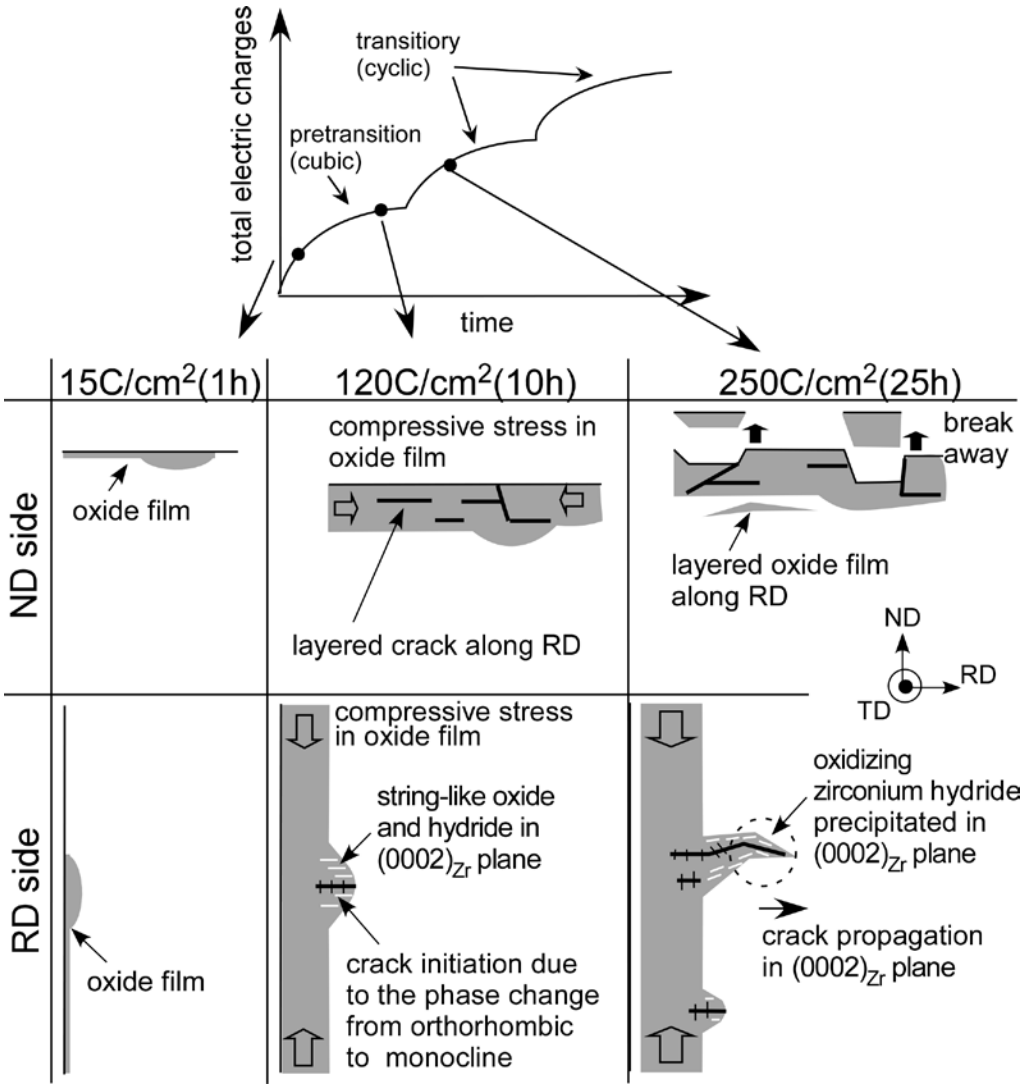

Figure 12 Schematic of the oxidation process of zirconium at 1.5 V and the mechanism of crack initiation and propagation in the (0002) plane in the zirconium matrix without an external stress.